

Optimal stretching in the reacting wake of a bluff body

Jinge Wang,¹ Jeffrey Tithof,¹ Thomas D. Nevins,² Rony O. Colón,¹ and Douglas H. Kelley¹

¹*Department of Mechanical Engineering, University of Rochester, Rochester, New York 14627, USA*

²*Department of Physics & Astronomy, University of Rochester, Rochester, New York 14627, USA*

(Received 14 September 2017; accepted 8 November 2017; published online 26 December 2017)

We experimentally study spreading of the Belousov-Zhabotinsky reaction behind a bluff body in a laminar flow. Locations of reacted regions (i.e., regions with high product concentration) correlate with a moderate range of Lagrangian stretching and that range is close to the range of optimal stretching previously observed in topologically different flows [T. D. Nevins and D. H. Kelley, *Phys. Rev. Lett.* **117**, 164502 (2016)]. The previous work found optimal stretching in a closed, vortex dominated flow, but this article uses an open flow and only a small area of appreciable vorticity. We hypothesize that optimal stretching is common in advection-reaction-diffusion systems with an excitation threshold, including excitable and bistable systems, and that the optimal range depends on reaction chemistry and not on flow shape or characteristic speed. Our results may also give insight into plankton blooms behind islands in ocean currents. *Published by AIP Publishing.*

<https://doi.org/10.1063/1.5004649>

In an advection-reaction-diffusion (ARD) system, the local concentration of a product species changes over time according to the combined effects of advection (flow), reaction (e.g., chemical reaction or biological growth), and molecular diffusion. Examples of ARD system include industrial chemical reactions,² forest fires,³ microfluidic reactors,⁴ combustion engines,^{5,6} and phytoplankton blooms.^{7–13} Even without advection, reaction and diffusion give rise to nonlinear phenomena like traveling waves and spiral waves,^{14–16} so including advection, which may be chaotic or turbulent itself, makes forecasting ARD systems a challenging task. But being able to forecast the spreading of the reacted region (where the concentration of the product species is high) and knowing how its edges will be constrained would allow better prediction of the concentration and uniformity of products in chemical reactors^{2,17} and microfluidic devices,¹⁸ more effective safety responses to forest fires,^{19,20} and better phytoplankton models for understanding Earth's carbon budget.^{12,21,22} In this paper, we present experimental measurements of an ARD system in the wake of a bluff body in a laminar channel flow. Reactive wakes are relevant to phytoplankton growth behind islands^{9,10} and slow zones in ARD in porous media,^{23–25} besides being interesting because they exhibit boundary layers and steep velocity gradients. We show that for this system with an excitation threshold, spreading of the reacted region is enhanced mostly where the local Lagrangian stretching falls within an optimal range, consistent with a prior result in a topologically different flow (closed alternating vortex flow).¹ Despite differences in flow field, the optimal range is similar. We hypothesize that the range depends on reaction kinetics and not on the details of advection, and will therefore apply to other flows as well.

fronts that separate reacted regions from unreacted ones. Because fronts have lower dimensionality than the space in which the reaction occurs (e.g., surfaces cutting through a volume of reacting fluid) and because fronts are drawn by reducing local concentration measurements to a binary (reacted or unreacted), fronts provide a more manageable representation of the system. Past studies have built a simplified characterization of ARD systems in which fronts advance through a combination of advection by the flow and diffusive transport, with the latter usually taken to be spatially uniform and temporally constant. It was shown that fronts moving according to this physics in steady or time-periodic flows are constrained by burning invariant manifolds (BIMs), which are one-way barriers the fronts cannot cross.^{26–28} BIMs were observed in experiment.²⁹ Later, the theory was generalized to flows of arbitrary time dependence, and the one-way barriers that arise in that context were called burning Lagrangian coherent structures (bLCS).³⁰ Tools for automated measurement of front speed and thickness at many locations throughout time and space have also been developed³¹ and are directly applicable to BIMs and bLCS. However, BIMs and bLCS reduce the chemical kinetics to a single value, the front speed, and any phenomena that emerge from reaction processes too intricate to be captured by that single value are necessarily neglected by these theories. Hence, there are some limitations to forecasting ARD systems using BIMs and bLCS.

Forecasting spreading is especially interesting and challenging in the regions near bluff bodies. Experiments have shown that ARD systems in porous media form reacted regions with sawtooth shapes.²³ Simulations reproduce the effect, and the shapes result from reacted regions becoming pinned in the slow zones behind individual grains in the porous medium,²⁴ that is, in wakes. Later experiments and simulations considering the flow around a single disc in a Hele-Shaw cell again found that the reacted region can be pinned near a bluff body, either upstream or downstream.²⁵

I. INTRODUCTION

One method for forecasting spreading in ARD systems is to simplify the problem by considering only the reaction

Involving little vorticity, the flow was well-modeled as potential flow. “Frozen fronts” have also been seen when spreading is inhibited by a headwind instead of a bluff body and explained in terms of BIMs.^{32,33} However, the frozen fronts near an obstacle required the front speed to depend on the front curvature,²⁵ and modifications to the normal BIM theory are needed to explain these.³³ Simulations have also shown how ARD dynamics can produce phytoplankton blooms in the wakes behind islands,^{9–11} similar to blooms observed in the ocean.

One recent study found that for a reaction with an excitation threshold, the product concentration tends to be highest where the Lagrangian stretching falls in an optimal range.¹ This effect cannot be explained by a simple modification of BIM and bLCS theories to incorporate a curvature dependence on front speed. An ARD system with an excitation threshold is one in which reaction proceeds if the local product concentration exceeds some threshold, but decays otherwise. The such simplest system is governed by the dynamics

$$\frac{\partial c}{\partial t} = -(\mathbf{u} \cdot \nabla)c + \alpha c(1 - c)(c - c_0) + D\nabla^2 c, \quad (1)$$

where c is the normalized product concentration, t is the time, \mathbf{u} is the flow velocity, α is the reaction rate, D is the material diffusivity of the product, and c_0 is the concentration threshold. The threshold c_0 is one example of a reaction parameter which is not captured when spreading is characterized using front speed alone. Marine phytoplankton growth may be governed by dynamics of this form.⁷ One example of ARD system with an excitation threshold is an *excitable* system, characterized by the additional fact that after being perturbed above the threshold, it eventually returns to the unperturbed state.^{34,35} Another example is a bistable system, which has two states that are both stable to small perturbations. In still other ARD systems, the second term on the right-hand side might take a different form, such as the second-order form $\alpha c(1 - c)$ first studied by Fisher,³⁶ which is has no threshold.

Reaction kinetics interacts with Lagrangian stretching in a way that affects growth. The Lagrangian stretching $S_t^{t+T}(\mathbf{x}_0)$ is defined as the square root of the maximum eigenvalue of the right Cauchy-Green strain tensor

$$\mathbf{C}_t^{t+T}(\mathbf{x}_0) = [\nabla \mathbf{F}_t^{t+T}]^\top [\nabla \mathbf{F}_t^{t+T}], \quad (2)$$

where \mathbf{x}_0 is the position and $\nabla \mathbf{F}_t^{t+T}$ is the gradient of the flow map between times t and $t + T$. The Lagrangian stretching has no units and is closely related to the finite-time Lyapunov exponents (FTLEs) $\lambda_t^{t+T} = \log(S_t^{t+T})/2T$. Roughly, for $T > 0$, $\lambda_t^{t+T}(\mathbf{x}_0)$ measures the exponential rate at which neighboring fluid elements at position \mathbf{x}_0 will separate due to advection, and $S_t^{t+T}(\mathbf{x}_0)$ measures the strain that will be experienced by a fluid element at \mathbf{x}_0 , within the time interval t to $t + T$. For $T < 0$, λ_t^{t+T} measures the exponential rate at which neighboring fluid elements have approached each other, and S_t^{t+T} measures the strain that was recently experienced by the fluid element.

Lagrangian stretching and FTLEs have been used extensively to approximate the locations of barriers to the movement of *non-reacting* species^{37–40} and are closely related to Lagrangian Coherent Structures,^{41,42} which are also calculated using \mathbf{C}_t^{t+T} . FTLEs have also been considered in ARD systems. Numerical experiments have shown that in double-gyre flow, a common model for mesoscale ocean dynamics, reaction rate is enhanced where FTLEs are large.⁴³ Similarly, if two reactions compete, the one that is triggered where FTLEs are smaller is eventually overwhelmed.^{2,44} Earlier experiments showed that the overall reaction rate increased when the average FTLE value increased.⁴⁵ However, recent evidence¹ suggests that strong stretching may *inhibit* the growth of reacted regions.

The recent study mentioned above¹ found an “optimal” range of Lagrangian stretching. The authors argued that for a reaction with an excitation threshold in an incompressible flow, non-zero stretching implies that fluid elements are simultaneously lengthening in (at least) one direction and contracting in (at least) one other. Therefore, S_t^{t+T} measures both the rate at which fresh reactants are brought to the reacted region and the rate at which the reacted region is diluted. The first process can enhance the local concentration c above the threshold c_0 , whereas the second can deplete it below threshold. An optimal range results from the balance between the two processes. The interaction of those two processes was noted previously in analytic flow models.^{46,47} This work, although consistent with these numerical studies, was based on a single experimental geometry—an array of alternating vortices. Neither bluff body was considered nor did those flows involve boundary layers or substantial shear (the vortex arrays were almost purely rotational).

In this article, we present experimental measurements of an ARD system in the wake of a bluff body in a laminar channel flow, considering both product concentration and Lagrangian stretching. Vorticity, boundary layers, and shear are all present. We find that a range of optimal stretching exists and that the range closely matches the range observed previously¹ despite the stark differences in the flow. Below, the paper proceeds as follows: In Sec. II, we describe the experimental apparatus and the methods for driving flow, exciting a reaction, and measuring the dynamics. We characterize the flow produced by the channel in some detail, since the device has not been described in the literature before. In Sec. III, velocity and stretching fields are characterized with the bluff body in place. Then, in Sec. IV, typical product concentration fields are presented and we identify the range of optimal stretching. Finally, we summarize the results and discuss their implications in Sec. V.

II. METHODS

We study flow along a polyvinyl chloride channel that is 640 mm long and 139 mm wide, as shown in Fig. 1. The channel contains a 4 mm-deep fluid layer which is leveled by measuring the layer depth on opposite ends with a ruler. Fluids inside the channel is driven by magnetohydrodynamic forcing. We induce flow by passing an electric current density \mathbf{J} through the fluid in the spanwise ($-y$) direction, in the

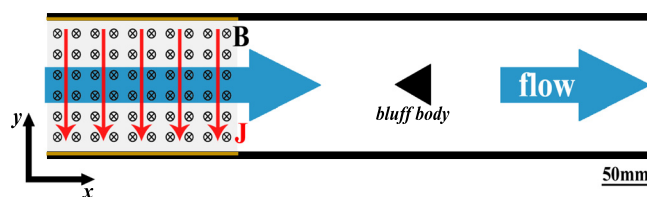


FIG. 1. Schematic of the channel flow apparatus, viewed from above. A thin layer of fluid is driven steadily along the length of the channel by electromagnetic forcing. In the drive section, at left, a cross-stream electric current density \mathbf{J} (indicated by red arrows) passes through the fluid in the presence of a downward magnetic field \mathbf{B} produced by nearby permanent magnets, causing streamwise Lorentz forces in the x -direction. We study advection-reaction-diffusion dynamics in the wake behind a bluff body, located far from the drive section and far from channel ends, on the channel center line.

presence of a downward ($-z$) magnetic field \mathbf{B} , such that a Lorentz force drives fluid in the streamwise direction x . The magnetic field is provided by rectangular ceramic magnets with size of $152\text{ mm} \times 102\text{ mm} \times 12.7\text{ mm}$, oriented with their largest dimension aligned in the spanwise direction y . Individually, each magnet produces a field with magnitude of 40 mT near the center of the face. However, to increase the magnetic field magnitude, we stack two magnets below the fluid layer and two above it. The resulting field strength near the center of the fluid layer is $B \sim 50\text{ mT}$, though the field has greater magnitude in its fringes near the magnet edges, as discussed below. The magnet stacks cover the 102-mm-long forcing section of the channel, where electrical current passes. After fluid exits the end of the channel as sketched in Fig. 1, it diverges and recirculates along the outside edges of both side-walls, being contained by a broad, flat pan that allows ample room for recirculation. Thus, experiments can be run continually over long durations with well-controlled flow speed and no moving parts. Despite the recirculation, the fluid flow can be considered open since we stop data measurement before fluid particles recirculate back to their initial regions in the data. Neither magnets nor current is present outside the forcing section. We take measurements in a central region, far from both the forcing section and the end of the channel, where the flow is quite uniform along the streamwise direction. The flow is nearly two-dimensional; though Ekman pumping⁴⁸ and shear instabilities⁴⁹ might cause vertical motion, both are minimized by the facts that rotation occurs only in wakes and that all experiments described below take place in the slow, steady regime.

The flowing fluid contains the ingredients for the ferroin-catalyzed Belousov-Zhabotinsky (BZ) reaction,^{50,51} an excitable reaction that is orange in its unreacted state and blue in its reacted state. We use the recipe given by Gowen and Solomon.⁵² The BZ reaction is also oscillatory, in which once it is excited into a reacted state, it will return to its unreacted state.⁵⁰ The timescale of each full oscillation is on the order of 300 s and therefore has negligible effect on the results described below, which occur on much shorter time-scales. We trigger the BZ reaction by inserting a silver wire into the fluid, typically near the center of the wake behind the bluff body, where circulation and relatively slow flow make it easier to trigger the reaction. The measured kinematic viscosity of the BZ solution is $\nu = 1.6 \times 10^{-6}\text{ m}^2/\text{s}$.¹

We measure the velocity field \mathbf{u} and product concentration field c simultaneously and throughout space using two hardware-synchronized cameras (Emergent HS-4000M), each recording images with pixel dimensions of 2048×2048 , resolution of $125\text{ }\mu\text{m}/\text{pixel}$, and frame rates sufficient to resolve all relevant dynamics of advection, reaction, and diffusion (60 Hz in the experiments discussed below). The cameras are fitted with 25 mm Fujinon CF25HA-1 lenses. We illuminate the apparatus with blue LEDs and fit one camera with a dichroic filter that blocks red but passes blue, such that blue reacted regions appear bright but orange unreacted regions appear dark. Thus, brightness provides a first-order measure of product concentration. The other camera measures the flow field via particle tracking velocimetry, using methods very similar to the prior work.⁴⁹ We image the motion of passive tracer particles (Cospheric UVPMS-BG-1.025, density of $1.022\text{ g}/\text{cm}^3$, diameter ranging from 90 to $100\text{ }\mu\text{m}$) which we add to the solution and whose motion closely matches that of the surrounding fluid. The particles absorb blue light and fluoresce green, so this camera is fitted with a dichroic filter that blocks blue but passes green, to reduce glare. The particle tracking algorithm^{53,54} locates each particle individually and tracks its motion through space and time, producing a velocity measurement at the location of each particle in each movie frame. In the experiments described below, we tracked an average of about $12\,000$ particles in each frame.

By varying the magnitude of the current I , we control the flow speed. Typical velocity profiles at six different current magnitudes are shown in Fig. 2. Each is calculated by tracking particles for 20 s , extracting all velocity measurements that fall in a 1 mm band across the channel, and averaging the streamwise velocity, conditioned on the spanwise location. Larger currents drive faster flow. The profiles indicate that the velocity is maximum close to the channel walls, with large velocity gradients near the maxima and small gradients at the center. These M-shaped profiles are typical of magnetohydrodynamically driven flow,^{55–58} and the fast regions near channel walls are caused by strong fringing fields at the magnet edges. The apparatus behaves much as we would expect. We note that our velocity measurements do not quite extend to the channel walls, where a no-slip boundary condition requires that the velocity go to zero.

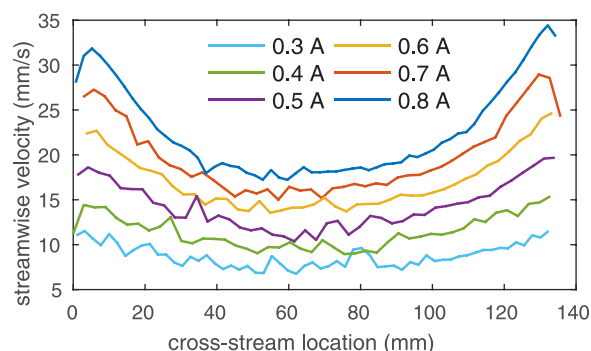


FIG. 2. Time-averaged velocity profiles of flow driven by various constant currents, without the presence of bluff body. Each profile is measured at the channel location marked by a dashed line in Fig. 6. Speed increases with current, and the profile shows the “M shape” typical in magnetohydrodynamically driven flows.

Since our interest here is ARD dynamics in the wake of a bluff body, we place a triangular bluff body (equilateral, with side length $L = 45$ mm and height greater than the fluid depth) downstream from the forcing section, symmetric on the channel center line, as shown in Fig. 1. Near the bluff body, no magnetohydrodynamic forces are present and the channel end is far away. We define the Reynolds number of the flow using the side length of the bluff body: $Re = UL/\nu$, where U is the root-mean-square velocity measured from particle tracking. When Re is large enough, the bluff body causes a recirculating wake. Boundary layers on the leading edges of the triangle separate at its sharp corners, resulting in a pair of vortices behind the bluff body, as is common in wakes. Though circular bluff bodies have been studied more often in the past,⁵⁹ we choose a triangular bluff body because it produces wakes at lower flow speeds that are closer to the $V = 72$ $\mu\text{m/s}$ speed at which BZ fronts advance in the absence of advection.³¹ If $U \gg V$, reaction becomes negligible and the ARD dynamics approach those of passive scalar mixing. We are interested in the regime where reaction is appreciable: $U \sim V$. While our flow speeds will be on average much higher than the front speed, the presence of a no-slip bluff body ensures that there will always be slow zones where $U \sim V$.

III. FLOW CHARACTERIZATION

Having discussed the apparatus and instrumentation in some detail, we proceed to discuss the characteristics of the flow. In the experiments considered here, we set $I = 0.8$ A, since it creates a large, well-defined, steady wake. The measured Reynolds number is $Re = 520$, and the recirculation period is 85 s. Figure 3 shows typical particle tracks. A recirculating wake composed of two vortices is visible, as are the elliptic stagnation points at the vortex centers. A hyperbolic stagnation point is visible on the flow center line, where fluid inside the vortices turns upstream, separating from fluid outside the vortices, which continues downstream. Particle tracks do not penetrate the bluff body. The wake is nearly

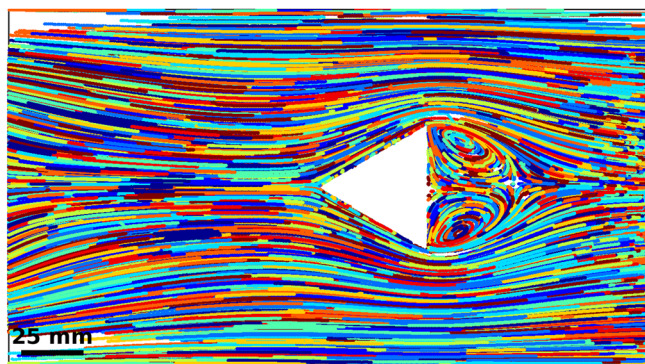


FIG. 3. Typical particle tracks observed in a bluff body experiment. These tracks are from a 5-s sampling of a longer experiment, and only tracks with duration greater than 1.67 s are plotted. Different colors indicate the paths of different particles. The drive current was 0.8 A. Elliptic and hyperbolic stagnation points are visible in the wake. Tracking a large number of particles produces high-resolution measurements that give access to intricacies of the flow.

symmetric (though symmetry is not essential for studying ARD dynamics in a wake).

Just as we characterized the velocity profile of the channel without the bluff body (Fig. 2), we can characterize the velocity profile with the bluff body in place. Figure 4 compares the two profiles, both with $I = 0.8$ A and both calculated by averaging velocity measurements within the same 1 mm band, as described above. We choose that band such that it passes through the elliptic stagnation points; the dotted-dashed red line in Fig. 6 indicates its location. The stagnation points are visible as zeroes in the streamwise velocity in Fig. 4, which occur only when the bluff body is present. Between the stagnation points, the streamwise velocity is negative, indicating recirculation. The presence of the bluff body reduces the effective width of the channel; due to conservation of mass, and the downstream speed increases in the regions between the channel walls and the bluff body. However, the two velocity profiles are similar near the channel walls. Boundary layer separation is seen, now indicated by the narrow, high-speed regions at the sharp corners of the bluff body. Some asymmetry in the velocity profiles is evident and likely results from imperfect leveling of the channel, which causes the layer depth to vary slightly from place to place. Thicker layers flow faster due to lower Rayleigh friction (dissipation due to the bottom of the container), which scales inversely with the square of the fluid layer thickness.⁶⁰ Still, as mentioned above, perfect symmetry is neither our goal nor essential for the topics of our interest.

When $Re = 520$, the flow is essentially steady. To quantify its time variation, we measure the root-mean-square velocity $\langle u^2 \rangle^{1/2}$ for each frame, where the brackets signify spatial averaging. As shown in Fig. 5, $\langle u^2 \rangle^{1/2}$ deviates little over time from its long-term mean value, 18.3 mm/s. The maximum difference is 0.168 mm/s (less than 1% of the mean), and the standard deviation is 0.0573 mm/s (0.3% of the mean). These tiny variations in time may be the result of a small number of incorrect measurements in the particle tracking algorithm, which is unavoidable with a high particle

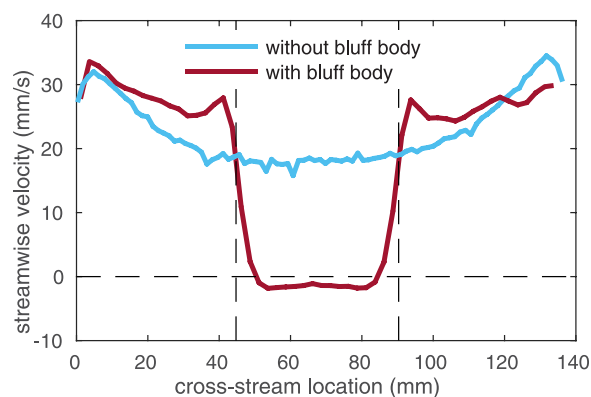


FIG. 4. Velocity profiles with and without the bluff body. Dashed vertical lines mark the spanwise extent of the bluff body. Each profile is calculated using the same averaging as in Fig. 2 along the dotted-dashed red line in Fig. 6. The drive current was 0.8 A in both cases. The bluff body causes recirculation in its wake and increases the streamwise velocity outside its wake, especially where boundary layers separate.

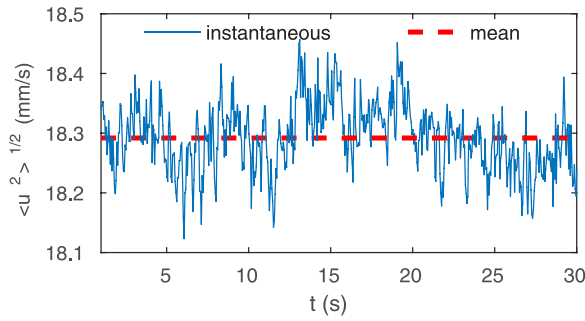


FIG. 5. Root-mean-square velocity as it varies over time, which indicates that the flow is essentially steady.

density. Regardless, we expect any instantaneous snapshot of the flow to closely match the temporal mean.

Because the flow is steady, we can combine particle tracks from different times to increase the effective spatial resolution of our velocity measurements, producing a single, high-resolution velocity field. However, since particle tracking produces measurements at the particle locations, which are irregular, combining the data requires more effort than a simple time average. We begin with 5.51×10^5 particle tracks recorded over 30 s, comprising 2.09×10^7 individual velocity measurements. Dividing that data into subsets each 2.5 s long, we interpolate all velocity measurements in each subset onto a common, rectangular grid with spacing

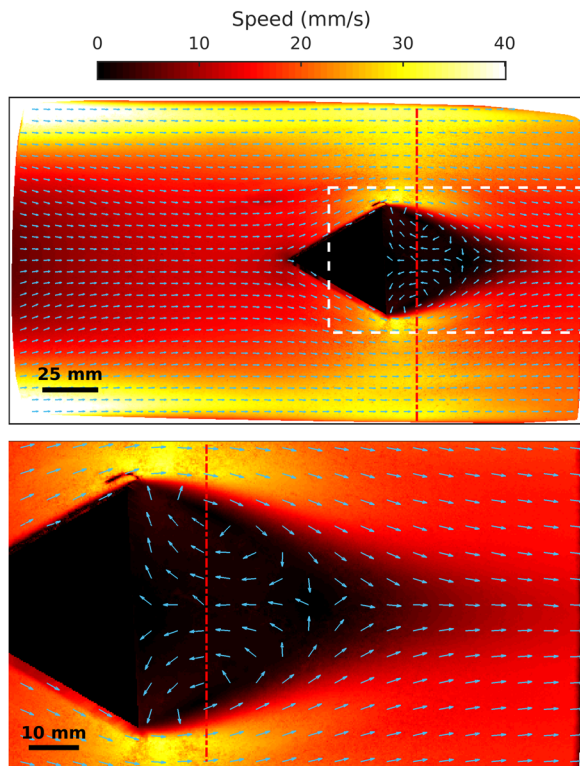


FIG. 6. Velocity field calculated by interpolating 20 s worth of particle tracks onto a uniform grid, then averaging over time. Top: the whole field of view excluding regions outside the channel. Arrows are unit vectors indicating the local flow direction, and the background color indicates speed. The vertical dotted-dashed red line marks the region used to calculate velocity profiles shown in Figs. 2 and 4. Bottom: Enlargement of the region bounded by the white dashed rectangle in the image at top, showing recirculation in the wake. Note that velocity vectors are downsampled for clarity.

$625 \mu\text{m}$. Once each subset has been interpolated onto the grid, we time-average their velocities, producing a mean velocity field with an average of 20 measurements per grid point. Figure 6 shows the result. Recirculation and stagnation points are clearly visible, consistent with Figs. 3 and 4.

From the velocity field, we can calculate the Lagrangian stretching S_t^{t+T} , as shown in Fig. 7 using three different values of the deformation time T . In all cases, $T < 0$, because the instantaneous reacted region can depend only on the past and not on the future. As the magnitude of T grows, the magnitude of S_t^{t+T} also grows, because fluid elements have more time to be deformed by advection. The spatial structure of the stretching field also becomes more clear as the magnitude of T increases, revealing first the wake edges, then the vortex edges. The boundary layer and its separation are evident and correspond to strong stretching. Another region of strong stretching lies near the center line between the vortices, starting near the hyperbolic stagnation point. As with the velocity, imperfect symmetry is apparent but unimportant. Stretching cannot be specified in the white regions, where fluid elements have not remained within the field of view for duration T . As the magnitude of T increases, white regions grow to fill nearly the entire field of view, but not the wake, where we expect ARD dynamics to be most interesting.

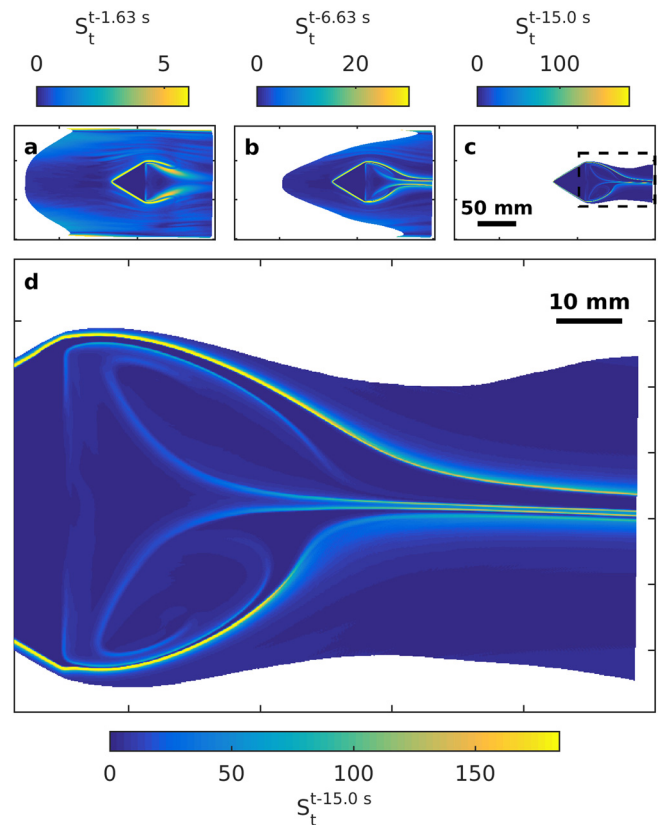


FIG. 7. Lagrangian stretching S_t^{t+T} of flow around a triangular bluff body. (a) Deformation time $T = -1.63$ s, (b) $T = -6.63$ s, (c) $T = -15.0$ s, and (d) enlargement of the region indicated by the black rectangle in (c), which is the same region shown in Fig. 6(b). As the deformation time T increases, the magnitude of the stretching also increases. Because the flow is steady, the time t is arbitrary. Regions of strong stretching occur at the edges of wake vortices and where boundary layers separate from the bluff body.

IV. OPTIMAL STRETCHING OF REACTION

In experiments, we first drive the flow for several seconds to clear any initial transients, and then we trigger a reaction in the wake and observe the reacted region as it spreads. We record data for a duration less than one circulation period such that the flow is essentially open rather than closed despite the recirculation. A series of snapshots from a typical experiment are shown in Fig. 8 (Multimedia view). The reacted region initially grows in the upper vortex, then spreads to the lower vortex and downstream along the boundary layer. Though the two vortices are separated by a barrier to the movement of non-reacting species (a manifold), the barrier does not apply to reacting species. The reacted region fails to spread beyond the edge of the wake, however. This characteristic shape typically persists until the BZ reaction oscillates back to its unreacted state (on a time-scale much longer than the dynamics of interest).

Our interest is in the role of stretching in ARD dynamics, so we seek to compare concentration fields like those shown in Fig. 8 (Multimedia view) to stretching fields like those shown in Fig. 7. First, however, we must choose a deformation time T . Typically, the spatial variation of S_t^{t+T} depends only weakly on T , as long as the magnitude of T is sufficiently large.⁶¹ The characteristic flow time in these experiments is $L/U = 2.4$ s. Prior work with the same BZ recipe used $T = -15$ s.¹ We choose $T = -15$ s to allow direct comparison to that work: by using the same deformation time, local stretching values can be compared quantitatively. Moreover, $T = -15$ s satisfies $|T| > L/U$. Here and below, we abbreviate S_t^{t-15s} as S where appropriate.

Figure 9 shows a snapshot of product concentration overlaid with the flow's stretching field. When both quantities are viewed together, it is evident that the regions of strong stretching which extend from the corners of the bluff body separate two distinct regions: a largely unreacted region outside and a largely reacted region inside the separated boundary layer. Furthermore, two curved lines of strong stretching extend near the center line of the bluff body and separate the reacted region into two halves [the two halves are especially apparent in Fig. 8 (Multimedia view)]. We observe that regions of high concentration do not occur where the stretching is very strong or very weak, but rather where it is moderate. This observation suggests an optimal range of S to enhance the spread of the BZ reaction, consistent with the previous works.^{1,46}

To quantify that claim, we can estimate the probability $p(\text{reacted}|S)$ that a region is reacted, conditioned on its local

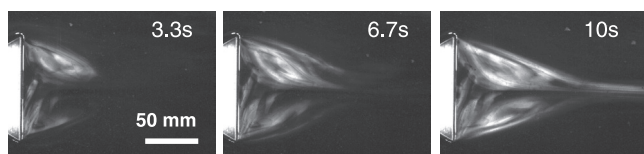


FIG. 8. Spreading of the reacted region over time in a typical experiment. Images are shown as recorded, with brighter shades indicating higher product concentration. (A small part of the white bluff body is also visible.) The time of each image is shown. As the reaction proceeds, the reacted region fills the wake vortices and grows downstream near the flow center line. Multimedia view: <https://doi.org/10.1063/1.5004649.1>.

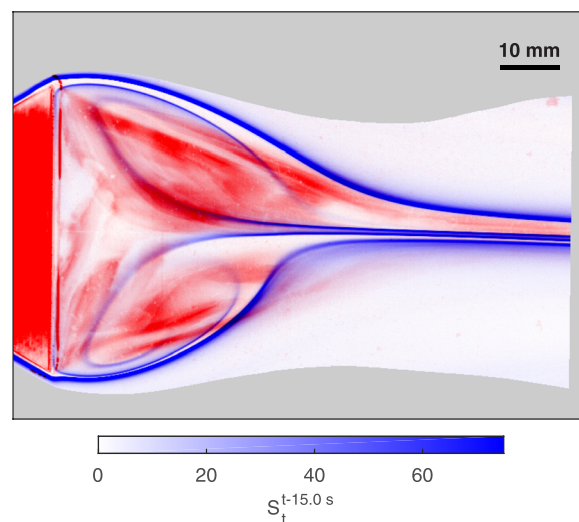


FIG. 9. Product concentration overlaid with stretching field. Shades of red indicate observed brightness, which measures product concentration. Redder regions correspond to higher concentration, except for within the triangular bluff body which also shows up on the reaction camera; the units are arbitrary. Shades of blue indicate stretching over deformation time $T = -15$ s. The field of view is the same as in Figs. 6(b) and 7(d). Stretching cannot be specified in the gray regions, where fluid elements have not remained long enough in the field of view. Highly reacted regions typically have moderate stretching, consistent with the hypothesis that an optimal range of stretching maximizes reaction rate.

stretching, as was done in the previous study.¹ For this calculation, we first choose a brightness threshold, defining all regions brighter than the threshold as being reacted and all regions dimmer than the threshold as being unreacted. Because the second Damköhler number is large, reacted regions are separated from unreacted regions by sharp fronts, so results depend only weakly on the choice of threshold. Typically, we choose the threshold to be 10% of the maximum brightness of the field of view, though other experiments with different lights and cameras would require a different criterion. Then, we calculate $p(\text{reacted}|S)$ as the ratio of the area that is both reacted and has stretching S to the total area with stretching S . Repeating this calculation for a range of S values produces the conditional statistics shown in Fig. 10. Note that we are careful to omit the interior of the bluff body from this calculation. These statistics come not just from the single snapshot of c shown in Figs. 8 (Multimedia view) and 9, but

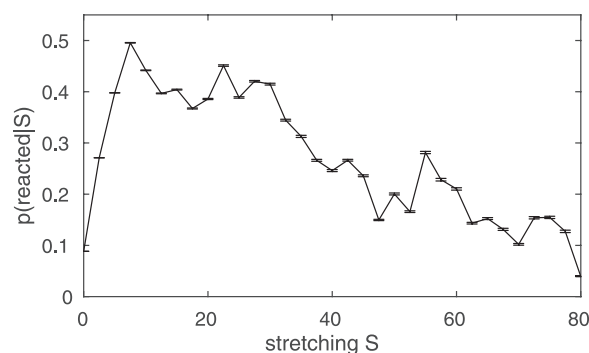


FIG. 10. The probability $p(\text{reacted}|S)$ that a region with a given stretching S will be reacted, based on our experiment. Error bars indicate uncertainty due to sample sizes.

from 17 s of observations encoded as 1021 images, ranging from the time when we trigger the reaction to the time when the reacted region returns to the field of view from upstream due to recirculation around the channel walls in the apparatus. The estimation error of p at specific S depends largely on the number of data points corresponding to the S value. Because S is weak in most regions,³⁸ estimation errors are higher where S is larger. Therefore, we eliminate stretching values with fewer than 20 000 data points, ensuring that at large S the estimation error is still relatively small. Our systematic uncertainty is much lower than in the prior work¹ because studying a steady flow makes gathering large data sets much easier.

As shown in Fig. 10, regions are unlikely to be reacted if the local stretching $S < 7.5$ or if the local stretching $S > 30$. That is, we observe that product concentration tends to be highest where the Lagrangian stretching falls within an optimal range, consistent with the prior work.¹ Because the prior work used $T = -15$ s just as we do, we can compare stretching quantitatively, and in fact the range is similar in both studies: in the previous study, optimal stretching occurred roughly for $8 \leq S \leq 20$, depending on the Reynolds number.¹ The fact that the optimal range contains slightly stronger stretching in this flow may be due to this flow having a significantly sharper gradient in the stretching field.

Finding even a rough quantitative match between the two flows seems remarkable, given that their Reynolds numbers, advective timescales, and topologies are so different. The prior study¹ considered quasi-two-dimensional flows driven electromagnetically using methods similar to those described above. The magnetic field, however, was not unidirectional but rather formed from a checkerboard array of magnets with alternating polarity, so that the low- Re flow was a checkerboard of vortices of alternating vorticity. Experiments spanned flow speed from $2 \text{ mm/s} \leq \langle u^2 \rangle^{1/2} \leq 15 \text{ mm/s}$, lower than the $\langle u^2 \rangle^{1/2} = 18 \text{ mm/s}$ experiments described above. The corresponding characteristic time scales spanned a range from 1.85 s to 11.5 s, some of which differ substantially from the 2.4 s timescale of the experiments described above. The vortex flows studied previously are characterized by a large number of stagnation points, tiled at vortex centers and between vortices, whereas the flow described above has stagnation points only in the wake. The vortex flows involve no boundary layers and almost no shear, but substantial vorticity throughout, all in contrast to the flow described above. And finally, some of the vortex flows change over time, unlike the flow described above. Advection processes differ in many ways, so one might not expect a measure like the one shown in Fig. 10 to match.

We explain the match in terms of local ARD dynamics. Global properties like root-mean-square speed, flow topology (number and arrangement of stagnation points), and the presence of boundary layers all differ substantially between the two studies. But the local ARD processes do not differ. Reaction kinetics and diffusivity match because the BZ recipe is unchanged. Since a chemical reaction front's dynamics can only depend on the advection local to it, the dynamics should not depend on the global flow properties. If stretching, S , is a dominant advection parameter, then we would

expect regions with the same S to behave similarly regardless of global properties, consistent with the resemblance between Figs. 9 and 10 and the corresponding figures in the prior study.¹ The mechanism for the influence of stretching is that a high stretching serves to distort reacted regions, thereby increasing surface area and enhancing diffusion. Enhanced diffusion assists a reaction by spreading catalyst quickly, but inhibits a reaction by reducing local concentration. In the case of a reaction with an excitation threshold, this dilution mechanism is thought to cause high stretching values to stop the propagation of reactions and lead to optimal stretching.^{1,46} Considering both sets of results, we hypothesize that optimal stretching is typical for ARD systems with excitation thresholds and that its range depends on reaction chemistry and not on flow shape or characteristic speed.

V. SUMMARY AND OUTLOOK

In summary, our study of excitable ARD dynamics in the wake of a bluff body has revealed that product concentration tends to be highest where Lagrangian stretching falls within an optimal range and that the range quantitatively agrees with earlier findings in a qualitatively different flow. To achieve our results, we constructed and characterized an experimental apparatus for driving channel flow in a thin fluid layer magnetohydrodynamically. The apparatus produces M-shaped velocity profiles as expected. Inserting a triangular bluff body produced a steady, well-defined wake with recirculating vortices. Using a large number of velocity measurements obtained from particle tracking velocimetry, we calculated Lagrangian stretching fields with high spatial resolution. We hypothesize that optimal stretching is typical for ARD systems with excitation thresholds and that its range depends primarily on reaction chemistry.

The mechanism that we use to create wakes and vortices is similar to the shading effect of islands in oceanic flow,^{10–12} which suggests the possibility of using Lagrangian stretching to forecast plankton blooms. Blooms often occur in the wakes behind islands. Predictions could be tested by calculating stretching from ocean models and comparing to satellite observations of chlorophyll concentration. Our observations are also consistent with the recent studies in laboratory and numerical experiments that found regions of high product concentration “frozen” near obstacles.^{24,25} It would be interesting to calculate stretching fields in those systems. In this study, we have considered one particular flow at one particular value of Re , carefully and in great detail. Though this open flow differs substantially from the closed flows considered in the prior work,¹ support for our hypothesis that optimal stretching is typical for ARD systems with an excitation threshold requires considering even more different flows. In particular, it would be interesting to observe ARD dynamics in a Von Kármán vortex street (in which vortices are periodically shed from a bluff body) to determine if optimal stretching occurs there. Wakes have been studied in great detail and are known to change shape dramatically as Re varies, so other shapes might also make for fruitful studies. Finally, it was noted already¹ that just as

regions of moderate stretching promote reaction, regions of strong stretching extinguish reaction, suggesting the possibility of “blowout barriers.” The regions of strong stretching evident in Figs. 7 and 9 along the center line and boundary layers appear to be blowout barriers and deserve future study.

ACKNOWLEDGMENTS

The authors gratefully acknowledge I. A. Mohammad, R. S. Russell, and B. F. Knisely for helpful comments and fabrication expertise. The Xerox Engineering Fellows Program at the University of Rochester supported R. O. Colón and partially supported J. Wang. The Discover Grant at the University of Rochester also partially supported J. Wang. T. D. Nevins was supported by the Department of Defense (DoD) through the National Defense Science & Engineering Graduate Fellowship (NDSEG) Program.

- ¹T. D. Nevins and D. H. Kelley, *Phys. Rev. Lett.* **117**, 164502 (2016).
- ²C. P. Schlick, P. B. Umbanhowar, J. M. Ottino, and R. M. Lueptow, *Chaos* **24**, 013109 (2014).
- ³C. Punckt, P. S. Bodega, P. Kaira, and H. H. Rotermund, *J. Chem. Educ.* **92**, 1330 (2015).
- ⁴T. M. Squires and S. R. Quake, *Rev. Mod. Phys.* **77**, 977 (2005).
- ⁵O. Kupervasser, Z. Olami, and I. Procaccia, *Phys. Rev. E* **59**, 2587 (1999).
- ⁶S. Liu and C. Tong, *Combust. Flame* **162**, 4149 (2015).
- ⁷J. E. Truscott and J. Brindley, *Bull. Math. Biol.* **56**, 981 (1994).
- ⁸A. P. Martin, *Prog. Oceanogr.* **57**, 125 (2003).
- ⁹M. Sandulescu, C. López, E. Hernández-García, and U. Feudel, *Nonlinear Proc. Geophys.* **14**, 443 (2007).
- ¹⁰M. Sandulescu, C. López, E. Hernández-García, and U. Feudel, *Ecol. Complex.* **5**, 228–237 (2008).
- ¹¹D. Bastine and U. Feudel, *Nonlinear Proc. Geophys.* **17**, 715 (2010).
- ¹²F. d’Ovidio, S. D. Monte, S. Alvain, Y. Dandonneau, and M. Lévy, *Proc. Nat. Acad. Sci. U. S. A.* **107**, 18366 (2010).
- ¹³Z. Neufeld, *Chaos* **22**, 037102 (2012).
- ¹⁴A. T. Winfree, *Science* **175**, 634 (1972).
- ¹⁵A. von Kameke, F. Huhn, G. Fernández-García, A. P. Muñozuri, and V. Pérez-Muñozuri, *Phys. Rev. E* **81**, 066211 (2010).
- ¹⁶A. von Kameke, F. Huhn, A. P. Muñozuri, and V. Pérez-Muñozuri, *Phys. Rev. Lett.* **110**, 088302 (2013).
- ¹⁷A. W. NIENOW, M. F. EDWARDS, and N. Harnby, *Mixing in the Process Industries*, 2nd ed. (Butterworth-Heinemann, 1997), Google-Books-ID: LxdFnHQcXhgC.
- ¹⁸K. S. Elvira, X. C. i. Solvas, R. C. R. Wootton, and A. J. deMello, *Nat. Chem.* **5**, 905 (2013).
- ¹⁹M. A. Finney, *For. Ecol. Management* **211**, 97 (2005).
- ²⁰B. Butler, R. Parsons, and W. Mell, in Proceedings of the Large Wildland Fires Conference (2015).
- ²¹T. Tél, A. de Moura, C. Grebogi, and G. Károlyi, *Phys. Rep.* **413**, 91 (2005).
- ²²W. H. Schlesinger, *Biogeochemistry: An Analysis of Global Change* (Academic Press, San Diego, 1991).
- ²³S. Atis, S. Saha, H. Auradou, D. Salin, and L. Talon, *Phys. Rev. Lett.* **110**, 148301 (2013).
- ²⁴S. Saha, S. Atis, D. Salin, and L. Talon, *Europhys. Lett.* **101**, 38003 (2013).
- ²⁵T. Chevalier, D. Salin, and L. Talon, *Phys. Rev. Fluids* **2**, 100 (2017).
- ²⁶J. R. Mahoney, D. Bargteil, M. Kingsbury, K. A. Mitchell, and T. H. Solomon, *Europhys. Lett.* **98**, 44005 (2012).
- ²⁷K. A. Mitchell and J. R. Mahoney, *Chaos* **22**, 037104 (2012).
- ²⁸J. R. Mahoney and K. A. Mitchell, *Chaos* **23**, 043106 (2013).
- ²⁹D. Bargteil and T. H. Solomon, *Chaos* **22**, 037103 (2012).
- ³⁰J. R. Mahoney and K. A. Mitchell, *Chaos* **25**, 087404 (2015).
- ³¹T. D. Nevins and D. H. Kelley, *Chaos* **27**, 043105 (2017).
- ³²P. W. Megson, M. L. Najarian, K. E. Lilienthal, and T. H. Solomon, *Phys. Fluids* **27**, 023601 (2015).
- ³³J. R. Mahoney, J. Li, C. Boyer, T. H. Solomon, and K. A. Mitchell, *Phys. Rev. E* **92**, 063005 (2015).
- ³⁴I. R. Epstein and J. A. Pojman, *An Introduction to Nonlinear Chemical Dynamics: Oscillations, Waves, Patterns, and Chaos*, Topics in Physical Chemistry (Oxford University Press, 1998).
- ³⁵Z. Neufeld and E. Hernández-García, *Chemical and Biological Processes in Fluid Flows: A Dynamical Systems Approach* (Imperial College Press, 2009).
- ³⁶R. A. Fisher, *Ann. Eugenics* **7**, 355–369 (1937).
- ³⁷G. Haller and A. C. Poje, *Physica D* **119**, 352 (1998).
- ³⁸G. A. Voth, G. Haller, and J. P. Gollub, *Phys. Rev. Lett.* **88**, 254501 (2002).
- ³⁹D. H. Kelley and N. T. Ouellette, *Phys. Fluids* **23**, 115101 (2011).
- ⁴⁰D. H. Kelley, M. R. Allshouse, and N. T. Ouellette, *Phys. Rev. E* **88**, 013017 (2013).
- ⁴¹M. R. Allshouse and T. Peacock, *Chaos* **25**, 097617 (2015).
- ⁴²G. Haller, *Annu. Rev. Fluid Mech.* **47**, 137 (2015).
- ⁴³W. Tang and C. Luna, *Phys. Fluids* **25**, 106602 (2013).
- ⁴⁴W. Tang and A. Dharmantara, *Phys. Fluids* **27**, 076601 (2015).
- ⁴⁵P. E. Arratia and J. P. Gollub, *Phys. Rev. Lett.* **96**, 024501 (2006).
- ⁴⁶Z. Neufeld, *Phys. Rev. Lett.* **87**, 108301 (2001).
- ⁴⁷Z. Neufeld, C. López, E. Hernández-García, and O. Piro, *Phys. Rev. E* **66**, 066208 (2002).
- ⁴⁸T. H. Solomon and I. Mezić, *Nature* **425**, 376 (2003).
- ⁴⁹D. H. Kelley and N. T. Ouellette, *Phys. Fluids* **23**, 045103 (2011).
- ⁵⁰S. K. Scott, *Oscillations, Waves, and Chaos in Chemical Kinetics* (Oxford University Press, Inc., New York, 1994).
- ⁵¹P. M. Wood and J. Ross, *J. Chem. Phys.* **82**, 1924 (1985).
- ⁵²S. Gowen and T. Solomon, *Chaos* **25**, 087403 (2015).
- ⁵³D. H. Kelley and N. T. Ouellette, *Am. J. Phys.* **79**, 267 (2011).
- ⁵⁴N. T. Ouellette, H. Xu, and E. Bodenschatz, *Exp. Fluids* **40**, 301 (2006).
- ⁵⁵J. I. Ramos and N. S. Winowich, *Phys. Fluids* **29**, 992 (1986).
- ⁵⁶S. Eckert, A. Cramer, and G. Gerbeth, *Magnetohydrodynamics* (Springer, The Netherlands, 2007), pp. 275–294.
- ⁵⁷M. Qin and H. H. Bau, *Phys. Fluids* **24**, 037101 (2012).
- ⁵⁸O. Zikanov, D. Krasnov, T. Boeck, A. Thess, and M. Rossi, *Appl. Mech. Rev.* **66**, 030802 (2014).
- ⁵⁹C. H. K. Williamson, *Annu. Rev. Fluid Mech.* **28**, 477 (1996).
- ⁶⁰B. Suri, J. Tithof, R. Mitchell, R. O. Grigoriev, and M. F. Schatz, *Phys. Fluids* **26**, 053601 (2014).
- ⁶¹S. C. Shadden, F. Lekien, and J. E. Marsden, *Physica D* **212**, 271 (2005).